2022 IEEE/RSJ International Conference on Intelligent Robots and Systems (IROS 2022)
October 23-27, 2022, Kyoto, Japan

Integrating Impedance Control and Nonlinear Disturbance Observer for Robot-Assisted Arthroscope Control in Elbow Arthroscopic Surgery*

Teng Li[1], Armin Badre[2], Hamid D. Taghirad[1,3], and Mahdi Tavakoli[1], *Senior Member, IEEE*

***Abstract*— Robot-assisted arthroscopic surgery is transforming the tradition in orthopaedic surgery. Compliance and stability are essential features that a surgical robot must have for safe physical human-robot interaction (pHRI). Surgical tools attached at the robot end-effector and human-robot interaction will affect the robot dynamics inevitably. This could undermine the utility and stability of the robotic system if the varying robot dynamics are not identified and updated in the robot control law. In this paper, an integrated framework for robot impedance control and nonlinear disturbance observer (NDOB)-based compensation of uncertain dynamics is proposed, where the former ensures compliant robot behavior and the latter compensates for dynamic uncertainties when necessary. The combination of impedance controller and NDOB is analyzed theoretically in three scenarios. A complete simulation and experimental studies involving three common conditions are then conducted to evaluate the theoretical analyses. A preliminary pHRI application on arthroscopic surgery is designed to implement the proposed framework on a robotic surgeon-assist system and evaluate its effectiveness experimentally. By integrating impedance controller with NDOB, the proposed framework allows an accurate impedance control when dynamic model inaccuracy and external disturbance exist.**

I. Introduction

Elbow arthroscopy is a novel and complex procedure that allows management of elbow stiffness, arthritis and fractures in a minimally fashion [1]. Minimally invasive surgery (MIS) has been gaining popularity due to its potential benefits of faster recovery time and decreased pain [2]. Recent advancements in surgical robotics are transforming the traditional orthopaedic surgeries and helping the surgeons generate more successful and precise surgical outcomes [3]–[5]. Furthermore, MIS has been adopted due to the widely used da Vinci robot system in more and more types of surgical operations [6], [7].

*This research is supported in part by the Canada Foundation for Innovation (CFI) under grants LOF 28241 and JELF 35916, in part by the Government of Alberta under grants IAE RCP-12-021 and EDT RCP-17-019-SEG, in part by the Government of Alberta's grant to Centre for Autonomous Systems in Strengthening Future Communities (RCP-19-001-MIF), in part by the Natural Sciences and Engineering Research Council (NSERC) of Canada under grants RTI-2018-00681, RGPIN-2019-04662, and RGPAS-2019-00106.

[1]T. Li, H. D. Taghirad, and M. Tavakoli are with the Department of Electrical and Computer Engineering, Faculty of Engineering, University of Alberta, Edmonton T6G 1H9, Alberta, Canada. E-mail: {teng4, h.taghirad, mahdi.tavakoli}@ualberta.ca

[2]A. Badre is with the Western Upper Limb Facility, Sturgeon Hospital, St. Albert, Alberta, Canada, and the Division of Orthopaedic Surgery, Department of Surgery, Faculty of Medicine & Dentistry, University of Alberta, Edmonton, Alberta, Canada. E-mail: badre@ualberta.ca

[3]H. D. Taghirad is with the Advanced Robotics and Automated Systems (ARAS), Industrial Control Center of Excellence, Faculty of Electrical Engineering, K. N. Toosi University of Technology, Tehran, Iran. E-mail: taghirad@kntu.ac.ir

In robot-assisted elbow arthroscopy, a robot can help to increase surgical accuracy and precision, *e.g.*, for bone alignment. It can also serve as an auxiliary surgical support, *e.g.*, to help surgeons reduce fatigue by holding the arthroscope [5]. In such a robot-assisted surgical support system, the robot dynamics can be dramatically affected due to the extra surgical tools attached onto the robot end-effector (EE) and the physical human-robot interaction (pHRI). Here both the mass of the surgical tools and the interaction force can be viewed as external disturbance. Therefore, an accurate estimation and compensation for dynamic uncertainties can be a critical step towards a stable and accurate control system.

Many methods have been proposed for estimating dynamic uncertainties and eliminating their effects on robot dynamics. A main solution is to design a linear or nonlinear disturbance observer (NDOB) which can monitor the dynamic uncertainties in real-time, and make a compensation when necessary. A comprehensive review on NDOB can be found in [8], and a historical review on versatile observers can be found in [9].

A classic first-order momentum observer and its variations of sliding mode momentum observers have been designed to estimate an external disturbance/force [10]. A disadvantage of these observers is that they require an accurate dynamic model and negligible/known friction torque for an accurate estimation. This makes sense since the observer usually estimates a lumped dynamic uncertainty term which includes both the dynamic model inaccuracy and the external disturbance/force. Therefore, only when the dynamic model is accurate, the estimation from the observer is of any accuracy. Additionally, the classic approach can provide exact estimation only when the external force is constant rather than time-varying.

A model-based extended state observer (ESO) [11] is used for estimating human-robot interaction force on an impedance-based three degrees-of-freedom (DOF) rehabilitation robot when a healthy subject and a post-stroke patient operates the robot separately. The effectiveness of ESO is demonstrated by simulation. However, as the authors analyzed, the experiment result on force estimation is not accurate enough due to the inaccurate dynamic model they used.

A NDOB observer is used to estimate constant external payloads on the robot EE of a 6-DOF WallMoBot [12]. Only 1-DOF is involved in the experiments for the sake of simplicity. The effectiveness of the NDOB observer has been demonstrated in that work.

As mentioned earlier, the output from an observer is a lumped uncertainty term that incorporates both the dynamic model inaccuracy and the external disturbances. In order

to have an accurate estimation on the external disturbances (*e.g.*, interaction force), the dynamic model inaccuracy (*e.g.*, friction) is better to be estimated independently. Research has focused on this issue by employing an additional observer. A neural network (NN) is utilized to reconstruct friction dynamics while a general momentum disturbance observer is used to estimate the external forces in [13]. The estimation accuracy on the external force is considerably improved since the friction is separately estimated by the NN. Similar approaches of combing a disturbance observer and a deep learning technique are also introduced in [14], [15].

Impedance control is widely used for human-robot collaboration due to its intrinsic property of compliance [16]. By an impedance controller, a robot can be controlled to be soft (compliant) or rigid (non-compliant) as necessary, which can ensure a safe human-robot interaction [17]. Furthermore, the measurement on the interaction force is not necessary for impedance control. Therefore, the sensor-free and compliance properties make it popular for surgical robots. One main issue for implementing an impedance controller is that it requires full knowledge of the robot dynamics whereas the identified dynamic parameters are usually inaccurate in practice. Note that admittance control, which can be viewed as a counterpart of impedance control, does require an external sensor to measure the interaction force though it does not require full knowledge of the robot dynamics [18].

During arthroscopic surgery, knowing the position and orientation of the arthroscope is critical for improving the surgeon's situational awareness by allowing the surgeon to know the relationship between the current field of view and the surgical pre-plan [19], [20]. A common way to monitor the position and orientation of the arthroscope is to employ a tracking system [21]. The drawback of using a tracking system is that the marker could be easily obstructed by the surgeon's body or other objects in the operating room. A robot-assisted surgical system is another promising solution where the coordinate system of the arthroscope-holding robot can be used for the tracking. Meanwhile, the robot can help to improve surgical accuracy and reduce the surgeon's effort by holding the arthroscope's weight. Developing such a robot-assisted surgical system as the physical user interface is meaningful both for a virtual surgical training simulator and for supporting the surgeon in live surgical procedures.

In our specific application of elbow arthroscopy MIS, an integrated framework consisting of impedance control and NDOB is constructed as illustrated in Fig. 1. In the proposed framework, the impedance control is selected to guarantee compliant robot behavior without using a force/torque sensor [16], while the NDOB is used to estimate dynamic uncertainties and compensate for them when necessary. In summary, the contributions of this paper are: (1) A novel framework for integrating impedance control and NDOB is proposed and the effectiveness is evaluated; (2) The combined output is analyzed in three scenarios, and evaluated by simulation and experimental studies.

The remainder of this paper is organized as follows: Section II is devoted to the description of impedance control and nonlinear disturbance observer as well as their combination. Section III presents simulations, experiments, and corresponding results in different conditions. A preliminary application scenario is presented in section IV to evaluate the effectiveness of the proposed framework in arthroscopic surgery. Section V gives the concluding remarks.

II. Methods

A. Robot dynamics and impedance control

A general dynamic model for an n-degree-of-freedom (DOF) rigid robot [22] can be given by

$$\mathbf{M}(\mathbf{q})\ddot{\mathbf{q}} + \mathbf{S}(\mathbf{q},\dot{\mathbf{q}})\dot{\mathbf{q}} + \mathbf{g}(\mathbf{q}) = \tau + \mathbf{J}^{\mathbf{T}}\mathbf{F}_{\mathbf{ext}} \tag{1}$$

where $\mathbf{M} \in \mathbb{R}^{n\times n}$ denotes the inertia matrix, $\mathbf{S} \in \mathbb{R}^{n\times n}$ denotes a matrix related to the Coriolis and centrifugal forces, $\mathbf{g} \in \mathbb{R}^n$ represents a gravity-related vector, $\tau \in \mathbb{R}^n$ is the commanded joint torque vector, $\mathbf{F}_{\mathbf{ext}} \in \mathbb{R}^6$ is the external force in Cartesian space, and $\mathbf{J} \in \mathbb{R}^{6\times n}$ is the Jacobian matrix. Note that friction is not included in (1).

A full impedance model [16], [17] for robot-environment contact can be expressed as

$$\mathbf{F}_{\mathbf{imp}} = \mathbf{M}_{\mathbf{m}}(\ddot{\mathbf{x}} - \ddot{\mathbf{x}}_{\mathbf{d}}) + \mathbf{D}_{\mathbf{m}}(\dot{\mathbf{x}} - \dot{\mathbf{x}}_{\mathbf{d}}) + \mathbf{K}_{\mathbf{m}}(\mathbf{x} - \mathbf{x}_{\mathbf{d}}) \tag{2}$$

where $\mathbf{M}_{\mathbf{m}}, \mathbf{D}_{\mathbf{m}}, \mathbf{K}_{\mathbf{m}}$ are user-designed matrices for inertia, damping, and stiffness, respectively. $\mathbf{x}_{\mathbf{d}}, \dot{\mathbf{x}}_{\mathbf{d}}, \ddot{\mathbf{x}}_{\mathbf{d}}$ are the desired position, velocity, and acceleration, respectively in Cartesian space, while $\mathbf{x}, \dot{\mathbf{x}}, \ddot{\mathbf{x}}$ are the actual robot position, velocity, and acceleration, respectively. $\mathbf{F}_{\mathbf{imp}} \in \mathbb{R}^6$ is the interacting wrench (force and torque) between the robot EE and the environment in Cartesian space.

To avoid the requirement for external force measurement, let us set the designed inertia matrix equal to the inherent inertia matrix of the robot, *i.e.*, $\mathbf{M}_{\mathbf{m}} = \mathbf{M}_{\mathbf{x}}$, where $\mathbf{M}_{\mathbf{x}}$ is the inherent inertia of the robot in Cartesian space and $\mathbf{M}_{\mathbf{x}} = \mathbf{J}^{-\mathbf{T}}\mathbf{M}\mathbf{J}^{-\mathbf{1}}$ [23]. By substituting (2) into (1) using $\mathbf{F}_{\mathbf{ext}} = \mathbf{F}_{\mathbf{imp}}$ and setting $\mathbf{M}_{\mathbf{m}} = \mathbf{M}_{\mathbf{x}}$, the first simplified version of impedance control law (V1) can be expressed as

$$\begin{aligned}\tau_{\mathbf{imp}} = \mathbf{M}\mathbf{J}^{-\mathbf{1}}(\ddot{\mathbf{x}}_{\mathbf{d}} - \dot{\mathbf{J}}\dot{\mathbf{q}}) + \mathbf{S}\dot{\mathbf{q}} + \mathbf{g} \\ +\mathbf{J}^{\mathbf{T}}[\mathbf{D}_{\mathbf{m}}(\dot{\mathbf{x}}_{\mathbf{d}} - \dot{\mathbf{x}}) + \mathbf{K}_{\mathbf{m}}(\mathbf{x}_{\mathbf{d}} - \mathbf{x})],\end{aligned} \tag{3}$$

where $\mathbf{J}^{-\mathbf{1}}$ will be replaced with the pseudo-inverse of the Jacobian $\mathbf{J}^{\#} = \mathbf{J}^{\mathbf{T}}(\mathbf{J}\mathbf{J}^{\mathbf{T}})^{-\mathbf{1}}$ when $\mathbf{J}$ is not a square matrix.

In order to represent a real mechanical system, a Coriolis and centrifugal term can be included into the impedance model (2). Accordingly, the augmented impedance model is

$$\begin{aligned}\mathbf{F}_{\mathbf{imp}} = \mathbf{M}_{\mathbf{x}}(\ddot{\mathbf{x}} - \ddot{\mathbf{x}}_{\mathbf{d}}) \\ +(\mathbf{S}_{\mathbf{x}} + \mathbf{D}_{\mathbf{m}})(\dot{\mathbf{x}} - \dot{\mathbf{x}}_{\mathbf{d}}) + \mathbf{K}_{\mathbf{m}}(\mathbf{x} - \mathbf{x}_{\mathbf{d}})\end{aligned} \tag{4}$$

where $\mathbf{S}_{\mathbf{x}}$ is the Coriolis and centrifugal matrix of the robot in Cartesian space and $\mathbf{S}_{\mathbf{x}} = \mathbf{J}^{-\mathbf{T}}\mathbf{S}\mathbf{J}^{-\mathbf{1}} - \mathbf{M}_{\mathbf{x}}\dot{\mathbf{J}}\mathbf{J}^{-\mathbf{1}}$. By substituting (4) into (1) using $\mathbf{F}_{\mathbf{ext}} = \mathbf{F}_{\mathbf{imp}}$, the second simplified version of impedance control law (V2) can be expressed as

$$\begin{aligned}\tau_{\mathbf{imp}} = \mathbf{M}\mathbf{J}^{-\mathbf{1}}(\ddot{\mathbf{x}}_{\mathbf{d}} - \dot{\mathbf{J}}\mathbf{J}^{-\mathbf{1}}\dot{\mathbf{x}}_{\mathbf{d}}) + \mathbf{S}\mathbf{J}^{-\mathbf{1}}\dot{\mathbf{x}}_{\mathbf{d}} + \mathbf{g} \\ +\mathbf{J}^{\mathbf{T}}[\mathbf{D}_{\mathbf{m}}(\dot{\mathbf{x}}_{\mathbf{d}} - \dot{\mathbf{x}}) + \mathbf{K}_{\mathbf{m}}(\mathbf{x}_{\mathbf{d}} - \mathbf{x})]\end{aligned} \tag{5}$$

Furthermore, for a set-point regulation problem, we set $\ddot{\mathbf{x}}_\mathbf{d} = \dot{\mathbf{x}}_\mathbf{d} = \mathbf{0}$. Then, the impedance control law V2 (5) can be simplified to V3 as expressed by (6), which is also known as task-space PD controller with gravity compensation.

$$\tau_\mathbf{imp} = \mathbf{J}^\mathbf{T}[\mathbf{K_m}(\mathbf{x_d} - \mathbf{x}) - \mathbf{D_m}\dot{\mathbf{x}}] + \mathbf{g} \tag{6}$$

The relationships among the three versions of the impedance control law V1, V2, and V3 are summarized as follows. All of the three versions avoid measuring external force by setting $\mathbf{M_m} = \mathbf{M_x}$. V1 is based on a general impedance model that is widely used in robotics control systems. V2 is based on an augmented impedance model that may represent a real mechanical system by including a Coriolis and centrifugal term into the model as shown in (4). V3 focuses on a specific set-point regulation problem based on V2. Therefore, V2 can be viewed as a bridge from V1 to V3, while V2 itself also represents an important simplification. For the subsequent simulations and experiments, only V2 and V3 are employed such that V2 can perfectly reduce to V3 when a set-point regulation problem is encountered. V1 was also implemented for testing but not reported here since no difference was found between V1 and V2 in terms of task performance.

B. Nonlinear disturbance observer

A nonlinear disturbance observer (NDOB) can be used to estimate all dynamic uncertainties as a lumped term [24], comprised of two categories. One is the dynamic model inaccuracy caused by inaccurate dynamic parameters (*e.g.*, friction, center of mass location, and link weight), while the other is the external disturbance (*e.g.*, extra payload attached onto the robot body, and robot-environment interaction force). From an analytical perspective, in the absence of external disturbance, the NDOB estimates the difference between the real dynamic model and the estimated dynamic model of the robot, and it can be expressed as

$$\begin{aligned}\tau_\mathtt{NDOB} &= -[(\mathbf{M} - \hat{\mathbf{M}})\ddot{\mathbf{q}} + (\mathbf{S} - \hat{\mathbf{S}})\dot{\mathbf{q}} + (\mathbf{g} - \hat{\mathbf{g}})] \\ &= -\Delta\mathbf{M}\ddot{\mathbf{q}} - \Delta\mathbf{S}\dot{\mathbf{q}} - \Delta\mathbf{g}\end{aligned} \tag{7}$$

where $\hat{\mathbf{M}}$, $\hat{\mathbf{S}}$, $\hat{\mathbf{g}}$ are the estimations on $\mathbf{M}$, $\mathbf{S}$, $\mathbf{g}$, respectively.

An adapted NDOB design based on [24]–[26] is used in this paper which can be expressed as

$$\begin{cases}\mathbf{L} = \mathbf{Y}\hat{\mathbf{M}}^{-1} \\ \mathbf{p} = \mathbf{Y}\dot{\mathbf{q}} \\ \dot{\mathbf{z}} = -\mathbf{L}\mathbf{z} + \mathbf{L}(\hat{\mathbf{S}}\dot{\mathbf{q}} + \hat{\mathbf{g}} - \tau - \mathbf{p}) \\ \tau_\mathtt{NDOB} = \mathbf{z} + \mathbf{p}\end{cases} \tag{8}$$

where $\mathbf{L} \in \mathbb{R}^{n\times n}$ is the observer gain matrix, $\mathbf{Y} \in \mathbb{R}^{n\times n}$ is a constant invertible matrix needs to be designed, $\hat{\mathbf{M}}$ is designed to be a symmetric and positive definite matrix and thus invertible, $\mathbf{z}$ is an auxiliary variable, $\mathbf{p}$ is an auxiliary vector determined from $\mathbf{Y}$, $\tau_\mathtt{NDOB}$ is the estimated lumped uncertainties via the NDOB observer. Note that the disturbance estimation error $\Delta\tau_\mathtt{NDOB} = \tau_\mathtt{NDOB} - \hat{\tau}_\mathtt{NDOB}$, *i.e.*, the difference between the real lumped uncertainties and the estimated lumped uncertainties, is globally uniformly ultimately bounded for this NDOB design according to [24], and will converge asymptotically to zero if the rate of change of the lumped uncertainties is negligible. For simplicity, in this paper we assume $\Delta\tau_\mathtt{NDOB} = 0$, *i.e.*, the NDOB can accurately estimate the exact difference between the real dynamic model and the estimated dynamic model. Therefore, we denote the NDOB output as $\tau_\mathtt{NDOB}$ instead of $\hat{\tau}_\mathtt{NDOB}$ in (8).

In (8), the first two equations are the specific user design on the vector $\mathbf{p}$ and matrix $\mathbf{L}$. The third equation is to update the auxiliary variable $\mathbf{z}$. The advantage of the adapted NDOB design is that it does not require acceleration measurement. Considering that designing an observer is not the focus in this paper, only summarized information about the adapted NDOB is introduced above. For a specific observer design methodology with detailed procedures, please refer to [24].

C. Integration of impedance controller and NDOB

In this section, we mathematically explore the outcome of the combination of impedance controller and NDOB. Three scenarios of the combination are considered according to the variations of the impedance control law introduced earlier.

In practice, for both the impedance control law and NDOB, the estimations of the dynamic coefficient matrices, *i.e.*, $\hat{\mathbf{M}}$, $\hat{\mathbf{S}}$, $\hat{\mathbf{g}}$ are used, due to the fact that their real values ($\mathbf{M}$, $\mathbf{S}$, $\mathbf{g}$) are unavailable.

Scenario 1, for impedance control law V1.
Using $\hat{\mathbf{M}}$, $\hat{\mathbf{S}}$, $\hat{\mathbf{g}}$, the combined outcome of the impedance control law V1 (3) and NDOB (7) can be given by

$$\begin{aligned}\hat{\tau}_\mathbf{imp} - \tau_\mathtt{NDOB} = &\underbrace{\mathbf{M}\mathbf{J}^{-1}\{\ddot{\mathbf{x}}_\mathbf{d} - \dot{\mathbf{J}}\dot{\mathbf{q}}\} + \mathbf{S}\dot{\mathbf{q}} + \mathbf{g} + \mathbf{P}\mathbf{D}}_{\tau_\mathbf{imp}} \\ &+ \underbrace{\Delta\mathbf{M}\mathbf{J}^{-1}(\ddot{\mathbf{x}} - \ddot{\mathbf{x}}_\mathbf{d})}_{residual}\end{aligned} \tag{9}$$

As shown in (9), the combined output is equal to the ideal impedance control law (*i.e.*, the impedance control law assuming full knowledge of robot dynamics) $\tau_\mathbf{imp}$ in (3) together with a residual term. This residual term is tending to zero as $\ddot{\mathbf{x}} \to \ddot{\mathbf{x}}_\mathbf{d}$, *e.g.* it is negligible when Cartesian acceleration tracking performance is accurate enough.

Scenario 2, for impedance control law V2.
Using $\hat{\mathbf{M}}$, $\hat{\mathbf{S}}$, $\hat{\mathbf{g}}$, the combined output of the impedance control law V2 (5) and NDOB (7) is calculated as

$$\begin{aligned}\hat{\tau}_\mathbf{imp} - \tau_\mathtt{NDOB} = &\underbrace{\mathbf{M}\mathbf{J}^{-1}\{\ddot{\mathbf{x}}_\mathbf{d} - \dot{\mathbf{J}}\mathbf{J}^{-1}\dot{\mathbf{x}}_\mathbf{d}\} + \mathbf{S}\mathbf{J}^{-1}\dot{\mathbf{x}}_\mathbf{d} + \mathbf{g} + PD}_{\tau_\mathbf{imp}} \\ &+ \underbrace{\Delta\mathbf{M}(\ddot{\mathbf{q}} - \ddot{\mathbf{q}}_\mathbf{d}) + \Delta\mathbf{S}(\dot{\mathbf{q}} - \dot{\mathbf{q}}_\mathbf{d})}_{residual}\end{aligned} \tag{10}$$

As shown in (10), the combined output is equal to the ideal impedance control law $\tau_\mathbf{imp}$ in (5) together with two residual terms. The two residual terms are tending to zero as $\ddot{\mathbf{q}} \to \ddot{\mathbf{q}}_\mathbf{d}$ and $\dot{\mathbf{q}} \to \dot{\mathbf{q}}_\mathbf{d}$, which means that they are negligible when the joint acceleration and velocity tracking are accurate enough.

Scenario 3, for impedance control law V3.
In this scenario, we assume that a steady state is achieved in set-point regulation, *i.e.*, $\dot{\mathbf{q}} = \ddot{\mathbf{q}} = \mathbf{0}$. Then using $\hat{\mathbf{M}}$, $\hat{\mathbf{S}}$,

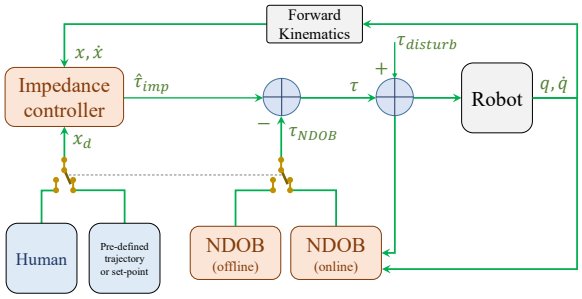

Fig. 1: Block diagram of the proposed control scheme with integrating impedance controller and nonlinear disturbance observer (NDOB). Note that the dashed line means a linked switch. $\tau_{\texttt{disturb}}$ is the dynamic model inaccuracy and the external disturbance.

$\hat{\mathbf{g}}$, the combined output of the impedance control law V3 (6) and NDOB (7) is calculated as

$$\begin{aligned}\hat{\tau}_{\mathbf{imp}} - \tau_{\texttt{NDOB}} &= \mathbf{J}^{\mathbf{T}}[\mathbf{K_m}(\mathbf{x_d} - \mathbf{x}) - \mathbf{D_m}\dot{\mathbf{x}}] + \hat{\mathbf{g}} - (-\mathbf{g} + \hat{\mathbf{g}}) \\ &= \underbrace{\mathbf{J}^{\mathbf{T}}[\mathbf{K_m}(\mathbf{x_d} - \mathbf{x}) - \mathbf{D_m}\dot{\mathbf{x}}] + \mathbf{g}}_{\tau_{\mathbf{imp}}}\end{aligned} \tag{11}$$

As shown in (11), the combined output is exactly equal to the ideal impedance control law $\tau_{\mathbf{imp}}$ in (6). This means that the NDOB can accurately compensate for inaccuracies in the estimation of the gravity term when the steady state is achieved in set-point regulation.

An integrated framework of impedance control and NDOB is proposed based on the analyses presented above. The block diagram of the control system is shown in Fig. 1 which incorporates the proposed framework.

III. Simulations, Experiments, and Results

A. Robotic system

A 3-DOF PHANToM Premium 1.5A robot (3D Systems, Inc., Cary, NC, USA) is used for simulations and experiments in this paper. For the simulations, we reconstruct the kinematic model and dynamic model of the PHANToM robot based on [27] and conduct the simulations using MATLAB/Simulink (version R2017a, MathWorks Inc., Natick, MA, USA). For the experiments, the physical robot is controlled via joint torque command, which is sent from MATLAB/Simulink using Quarc real-time control software (Quanser Inc., Markham, ON, Canada). The control rate of the robot is $1,000$ Hz. The MATLAB/Simulink and Quarc software run on a computer with a 3.33 GHz Intel(R) Core(TM) 2 i5 CPU with a Windows 7 Enterprise 64-bit operating system.

B. Parameterization

For all simulations and experiments in the remaining part of this paper, the parameter values used in the impedance model and NDOB are listed in Table I. In order to have a simple but natural movement, a circular and cyclic trajectory

TABLE I: Parameterization for simulation, experiment, and application of pHRI on elbow arthroscopic surgery simulator.

Parameters	Simulation	Experiment	pHRI Application
Spring	$\mathbf{K_m} = \mathbf{7.5I}$		$\mathbf{K_m} = \mathbf{0}$
Damping	$\mathbf{D_m} = \mathbf{2\sqrt{7.5}I}$		$\mathbf{D_m} = \mathbf{7.5I}$
Inertia matrix	$\hat{\mathbf{M}} = \mathbf{1.0 \times 10^{-3} \times I}$		
Observer gain	$\mathbf{Y} = \mathbf{9.58 \times 10^{-3} \times I}$		

Note: $\mathbf{I} \in \mathbb{R}^{3\times3}$ denote identity matrix.

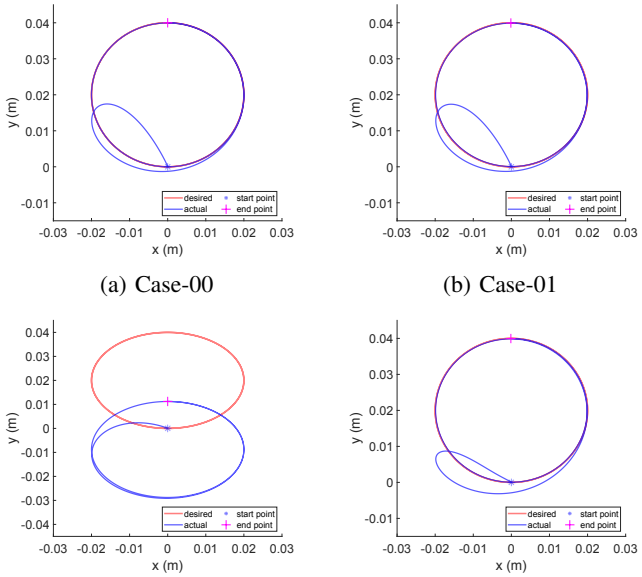

(a) Case-00 (b) Case-01

(c) Case-10 (d) Case-11

Fig. 2: Simulation results of the four cases of a circle tracking task in free space in Condition 1.

is selected for the simulations and experiments, which can be expressed as a function of time as the following

$$\begin{cases} x_d = R\sin(\frac{2\pi}{t_1}t) \\ y_d = R\cos(\frac{2\pi}{t_1}t) + R \\ z_d = 0 \end{cases} \tag{12}$$

where $R = 0.02$ m is the radius of the circle and $t_1 = 5$ s is the period for generating a full cycle.

In the following sub-sections, three conditions related to the combination of impedance controller and NDOB are presented. Both simulation and experimental results are included for each condition. The experiments are shown in the attached video[1].

C. Condition 1: Constant payload

Simulation

In Condition 1, a constant payload of 22 g is attached onto the robot EE as external disturbance, and there is no dynamic model inaccuracy involved. A circle tracking task in free space is employed and the circle trajectory is given by (12). This condition is performed by implementing the

[1]online video: https://drive.google.com/file/d/1kO5bhTbCwjgBDIsHyy22EkwMozGQGr5H/view?usp=sharing

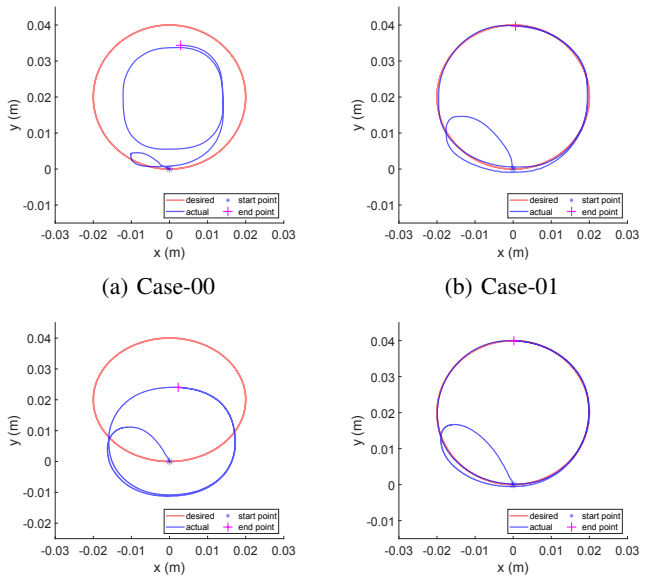

(a) Case-00 (b) Case-01

(c) Case-10 (d) Case-11

Fig. 3: Experimental results of the four cases of a circle tracking task in free space in Condition 1.

impedance control law V2 and NDOB, *i.e.*, the Scenario 2 given by (10). Four cases are designed for this condition:

- Case-00: External disturbance OFF, NDOB OFF;
- Case-01: External disturbance OFF, NDOB ON;
- Case-10: External disturbance ON, NDOB OFF;
- Case-11: External disturbance ON, NDOB ON.

The trajectory tracking results of the simulations are shown in Fig. 2. Note that no dynamic model inaccuracy is involved in the simulations, which means that the only dynamic uncertainty is the external disturbance of the constant payload. As can be seen in Fig. 2a, 2b, without the disturbance of the constant payload, the tracking results are the same no matter the NDOB is implemented or not. When the payload is attached as shown in Fig. 2c, the actual tracking trajectory deviates largely from the desired one if the NDOB is not implemented. However, by implementing a NDOB as shown in Fig. 2d, the disturbance from the constant payload can be fully detected and compensated for, thus good tracking performance is recovered. Note that there is a deviation between the actual trajectory and the desired trajectory at the beginning of the task. The reason is that their initial positions are not exactly the same. To this point, a low-pass infinite impulse response (IIR) filter can be implemented as necessary to ensure the smoothness of the movement at the beginning of the task.

Experiment

Similar to the simulations, experiments on the four cases are conducted by implementing the impedance controller and NDOB on a 3-DOF PHANToM robot. The experimental results of the four cases are shown in Fig. 3.

As can be seen in Case-00 (Fig. 3a), the circle tracking performance is poor. The reason is that dynamic model inaccuracies do exist (*e.g.*, joint friction) for the physical robot. As expected, when a NDOB is implemented in Case-01, this dynamic model inaccuracy is compensated for, and tracking performance is back to normal as shown in Fig. 3b. For Case-10 and Case-11, the experimental results similar to the corresponding simulation are obtained, *i.e.*, without NDOB, the tracking task fails due to the external payload as well as the model inaccuracy (Fig. 3c), while with NDOB, good tracking performance is recovered (Fig. 3d). Note that, here the NDOB in Case-11 has detected both the dynamic model inaccuracy (*e.g.*, joint friction) and the external disturbance (*i.e.*, the constant payload).

D. Condition 2: Time-varying payload

Simulation

In the simulation part of Condition 2, two types of time-varying payload are investigated. One is sinusoidal payload while another is a suddenly added constant payload. The former is to simulate a scenario of time-varying contact force during bone debridement while the latter is to simulate a scenario of sudden contact force when the tool hits a bone.

The same circle tracking task (12) is employed, whereas only Case-10 and Case-11 are considered. This condition is also performed by implementing the impedance control law V2 and NDOB, *i.e.*, the Scenario 2 given by (10). No dynamic model inaccuracy is involved in the simulations here.

The sinusoidal payload is applied onto the robot EE as external disturbance which can be expressed by

$$\begin{cases} Fx_d = a_1 \sin(\frac{2\pi}{t_1} t) \\ Fy_d = a_2 \sin(\frac{2\pi}{t_2} t) \\ Fz_d = a_3 \cos(\frac{2\pi}{t_3} t) \end{cases} \tag{13}$$

where $t_1 = 2$, $t_2 = 5$, $t_3 = 2$ are cycles of the desired time-varying EE payload for each axis in units of second, and $a_1 = 0.01$, $a_2 = 0.2$, $a_3 = 0.01$ are the corresponding amplitudes in units of Newton.

The simulation results of Condition 2 with a sinusoidal payload are shown in Fig. 4. As can be seen in Fig. 4a (Case-10), without NDOB, the tracking performance is distorted due to the sinusoidal payload. By implementing NDOB, normal tracking performance is obtained as shown in Fig. 4b (Case-11). The tracking performance with NDOB in Case-11 is shown in Fig. 4c, and the disturbance estimation on the external payload from the NDOB is shown in Fig. 4d.

The simulation results of Condition 2 with a suddenly added payload are shown in Fig. 5. In this simulation, a constant payload of 22 g is attached at the robot EE throughout the task, while another payload of 23 g is suddenly added onto the robot EE at 5.5 s and remains there since then. This procedure can be easily identified in Fig. 5a where the actual tracking trajectory is deviated due to the two payloads when NDOB is not activated. When the NDOB is activated, the tracking performance is well-recovered as shown in Fig. 5b and Fig. 5c. And the NDOB can immediately and accurately estimate the suddenly added payload as shown in Fig. 5d. The simulation results in Condition 2 demonstrate that the NDOB is able to accurately estimate the external time-varying disturbances in real-time as well.

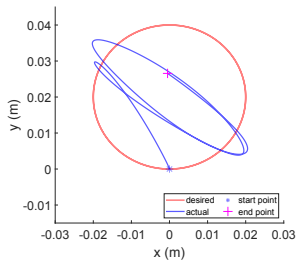

(a) Case-10 without NDOB

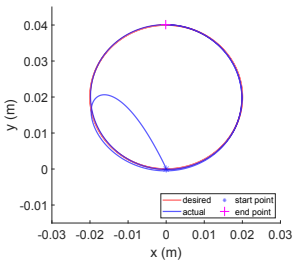

(b) Case-11 with NDOB

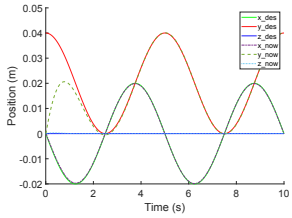

(c) Case-11 tracking result

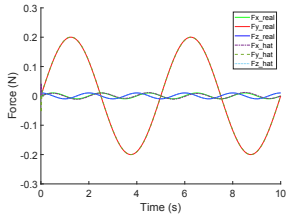

(d) Case-11 NDOB estimation

Fig. 4: Simulation results of a circle tracking task with sinusoidal time-varying payload in Condition 2.

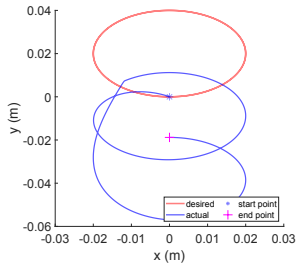

(a) Case-10 without NDOB

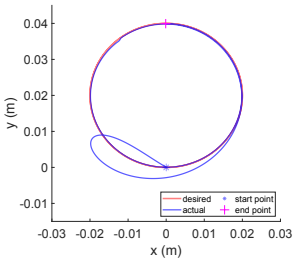

(b) Case-11 with NDOB

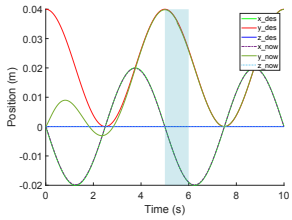

(c) Case-11 tracking result

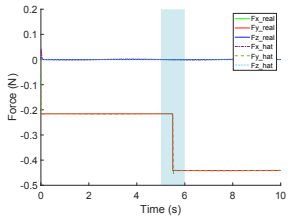

(d) Case-11 NDOB estimation

Fig. 5: Simulation results of a circle tracking task with a suddenly added payload (23 g) in Condition 2. Note that the 23 g payload is added at 5.5 s and remains there since then.

Experiment

For the experiment part of Condition 2, since it is impossible to apply a sinusoidal payload of (13) in practice, only an experiment with the suddenly added payload is performed. In the experiment, an extra magnetic constant payload of 23 g is added onto the robot EE in the middle of the circle tracking task. Note that a constant payload of 22 g is always attached at the robot EE in this experiment.

The experimental results of Condition 2 are shown in Fig. 6. As can be seen in Fig. 6a, only a small perturbation is observed immediately after the extra magnetic payload is added

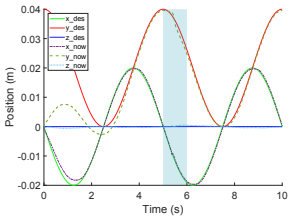

(a) Case-11 tracking result

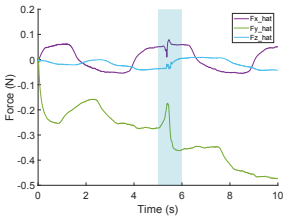

(b) Case-11 NDOB estimation

Fig. 6: Experimental results of a circle tracking task with a suddenly added payload (23 g) in Condition 2. An extra magnetic payload of 23 g is added onto the robot EE at some time point during 5-6 s (the colored area) in practice, and it remains there since then.

and good tracking performance is recovered very quickly. In Fig. 6b, the estimated force component F_y from NDOB is not piecewise constant compared with its corresponding simulation in Fig. 5d. The main reason should be that the estimation from NDOB in the physical experiment (Fig. 6b) involves both dynamic model inaccuracy and external payloads, while in the simulation (Fig. 5d) it involves only external payloads.

The experimental results in Condition 2 indicate that the NDOB is able to immediately detect and accurately compensate for a time-varying payload, thus protect the tracking performance from being affected. This verified the corresponding simulation results.

E. Condition 3: Set-point regulation

Simulation

In Condition 3, a set-point regulation problem is explored. The coordinates of the initial point and the desired set-point in Cartesian space are $[0, 0, 0]$ m and $[0.01, 0.04, 0]$ m, respectively. This condition is performed by implementing the impedance control law V3 and NDOB, *i.e.*, the Scenario 3 given by (11). Only Case-10 and Case-11 are considered. For both simulation and experiment in Condition 3, a constant payload of 22 g is always attached at the robot EE. Additionally, during the set-point regulation, an external disturbance force in a range of $[0, 2]$ N is applied onto the robot EE along $y+$ axis. In the simulation, the external disturbance is designed by (13) with a_1=a_3=0, a_2=t_2=2, which means that this time-varying disturbance is along y-axis and the maximum amplitude is 2 N. The external disturbance is applied only in the period of 6-7 s in the simulation.

The simulation results of Condition 3 are shown in Fig. 7. As can be seen in Case-10 (Fig. 7a), without NDOB, the regulation is failed with a large constant error between the desired (solid red line) and actual (dashed green line) set-point along y-axis. Here note that, even if with a higher stiffness in the impedance controller in Case-10, a constant error will still be remained if the gravity term cannot be appropriately compensated for. With NDOB in Case-11 (Fig. 7b), the regulation task achieves good performance.

For the external disturbance during 6-7 s (the colored area in Fig. 7), without NDOB, a large deviation as high

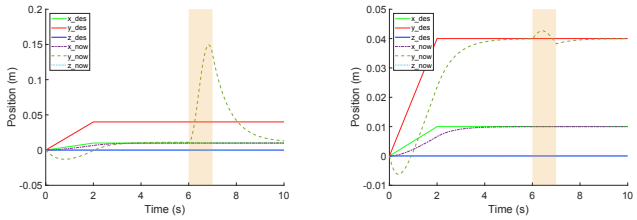

(a) Case-10 without NDOB (b) Case-11 with NDOB

Fig. 7: Simulation results of a set-point regulation task with a constant payload and 1s-disturbance in Condition 3. Note that, during the first two seconds, the desired point position is linearly increased to the final desired point position to ensure a smooth robot behavior at the moment of startup.

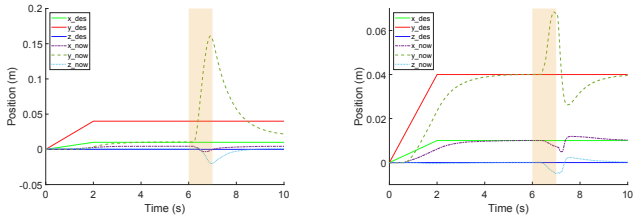

(a) Case-10 without NDOB (b) Case-11 with NDOB

Fig. 8: Experimental results of a set-point regulation task with a constant payload and 1s-disturbance in Condition 3. Note that the 1s-disturbance here is not exactly occurred during 6-7 s for 1 s since it is controlled by a human user.

as 14 cm is observed. But with NDOB, the deviation is significantly reduced to be less than 0.5 cm. This confirms the NDOB capability for disturbance rejection. The constant payload and the extra 1s-disturbance can be appropriately compensated for by using NDOB.

Experiment

For the corresponding experiment in Condition 3, the 1s-disturbance in a range of $[0, 2]$ N is exerted by a human user. Therefore, it is not exactly occurred during 6-7 s and not strictly lasted for 1 s in practice. The experimental results are shown in Fig. 8. As can be seen from the figure, the NDOB is able to minimize the effect induced by the external 1s-disturbance, which experimentally verified the corresponding simulation results. The results of Condition 3 indicate that the NDOB is also able to perform external disturbance rejection. From another perspective, the NDOB might undermine the compliant behavior brought by the impedance controller to some extent due to the disturbance rejection effect.

IV. Application on Elbow Arthroscopic Surgery

The simulation and experimental results of the three conditions in the previous section demonstrate that the NDOB is capable of accurately estimating dynamic uncertainties of both constant (Condition 1) and time-varying (Condition 2) payloads attached at the robot EE, and performs suitable compensation in the control system as necessary. The NDOB has a intrinsic property to reject external disturbance no matter the disturbance is expected or not (*e.g.*,

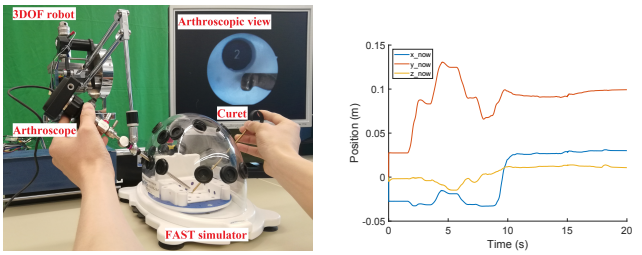

(a) Setup (b) Free trajectory

Fig. 9: Setup and free trajectory for implementing the proposed framework. FAST, fundamentals of arthroscopic surgery training. The robot and arthroscope are connected via a ball joint.

the 1s-disturbance in Condition 3). However, some human-generated disturbance, *e.g.*, human-robot interaction force, may be expected thus shouldn't be rejected. To solve this problem, NDOB-online and NDOB-offline are designed as shown in Fig. 1. With NDOB-online, a lumped dynamic uncertainties is estimated and compensated in real time, *i.e.*, all uncertainties will be rejected as disturbance. With NDOB-offline, only an appropriate constant gravity is compensated for which enables the human-robot interaction. Please note that this online/offline design is just what we needed since we do not want the robot to be compliant to occasional external disturbances when it is holding the tool still. One limitation here is that rigorous stability analysis has to be conducted in future work since controller online-switching is involved.

In a specific application on elbow arthroscopic surgery, a robot will hold the arthroscope as an auxiliary supporter to reduce the surgeon's fatigue. More specifically, when the surgeon moves the arthroscope, the robot should provide compliant behavior while complying with the external human-robot interaction force but compensating all other uncertainties. This can be realized via NDOB-offline. On the other hand, when the arthroscope is left in an unattended state, the robot should keep it stably stay there and be able to reject any external disturbance. This can be realized via NDOB-online. This illustrates the integrated framework in our specific application scenario. To this end, a practical application on the robot-assisted arthroscopic surgery is developed to assess the framework. In the application, it is expected that the proposed control system allows the surgeon to move the arthroscope freely and keeps the arthroscope stay still wherever the surgeon left it. A FAST simulator, as shown in Fig. 9a, is employed in the application where FAST is short for Fundamentals of Arthroscopic Surgery Training which is a commonly used physical model for training novices with their arthroscopic surgical skills. By implementing the framework, the arthroscope can move freely and stay in the air as shown in Fig. 9b.

Although this is a preliminary experiment, it is an important step towards constructing a robot-assisted elbow arthroscopic system. The results of this paper enable the system to accurately estimate and compensate for the robot

dynamic uncertainties for a stable control system. Also, the robot holds the arthroscope for the surgeons such that they can focus on other tasks during the surgery. In future work, the tool pose tracked by the marker-free robot system can be visualized and provided to the surgeons in real-time. More practically, the robot-assisted system can be used either for a training simulator by integrating with a virtual/phantom patient body via AR/VR techniques, or in real elbow arthroscopic surgery. The system is also promising to help guide the surgeon to perform tasks precisely and accurately, and to expand the application of elbow arthroscopy into various elbow conditions.

V. Conclusions

Robot-assisted arthroscopic surgery is a thriving field in orthopaedics. To build control system for a surgeon-assist arthroscope-holding robot, dynamic uncertainty is a critical point that needs to be estimated and compensated for during pHRI to ensure the system stability and accuracy. This paper proposed an integrated framework of combining impedance control and nonlinear disturbance observer (NDOB). The combined outcomes were mathematically analyzed. Three common conditions were presented to evaluate the combined outputs by both simulations and experiments on a 3-DOF PHANToM robot. A preliminary application of pHRI on elbow arthroscopic surgery simulator was realized by implementing the proposed framework, and its effectiveness was demonstrated. The core contribution of this paper is that, by combining impedance control and NDOB, the integrated framework can achieve an accurate impedance control under condition of that external uncertainties exist while only roughly estimated dynamic parameters are known.

The integrated framework is able to provide compliant behavior by the impedance controller during pHRI while compensating for the robot dynamic uncertainties by the NDOB. The NDOB used in this paper estimates a lumped value for model inaccuracy and external disturbance, and is not able to separate them. In future work, we will try to separate the interaction force from the lumped term by introducing additional observers or learning techniques into our system.

References

[1] K. Bennett and S. Kamineni, "History of elbow arthroscopy," *Journal of Arthroscopic Surgery and Sports Medicine*, vol. 1, no. 1, pp. 23–31, 2020.

[2] M. G. Fujie and B. Zhang, "State-of-the-art of intelligent minimally invasive surgical robots," *Frontiers of Medicine*, vol. 14, no. 4, pp. 404–416, 2020.

[3] R. H. Taylor *et al.*, *Medical Robotics and Computer-Integrated Surgery*. Cham: Springer International Publishing, 2016, pp. 1657–1684.

[4] D. J. Jacofsky and M. Allen, "Robotics in arthroplasty: a comprehensive review," *The Journal of arthroplasty*, vol. 31, no. 10, pp. 2353–2363, 2016.

[5] J. M. McDonnell *et al.*, "Surgeon proficiency in robot-assisted spine surgery: a narrative review," *The bone & joint journal*, vol. 102, no. 5, pp. 568–572, 2020.

[6] J. C. Garcia Jr and E. F. de Souza Montero, "Endoscopic robotic decompression of the ulnar nerve at the elbow," *Arthroscopy Techniques*, vol. 3, no. 3, pp. e383–e387, 2014.

[7] C. D'Ettorre, A. Mariani *et al.*, "Accelerating surgical robotics research: Reviewing 10 years of research with the dVRK," *arXiv preprint arXiv:2104.09869*, 2021.

[8] A. Mohammadi, H. J. Marquez, and M. Tavakoli, "Nonlinear disturbance observers: Design and applications to Euler-Lagrange systems," *IEEE Control Systems Magazine*, vol. 37, no. 4, pp. 50–72, 2017.

[9] A. Radke and Z. Gao, "A survey of state and disturbance observers for practitioners," in *2006 American Control Conference*. IEEE, 2006, pp. 6 pp.–.

[10] G. Garofalo *et al.*, "Sliding mode momentum observers for estimation of external torques and joint acceleration," in *2019 International Conference on Robotics and Automation (ICRA)*. IEEE, 2019, pp. 6117–6123.

[11] G. Sebastian *et al.*, "Interaction force estimation using extended state observers: An application to impedance-based assistive and rehabilitation robotics," *IEEE Robotics and Automation Letters*, vol. 4, no. 2, pp. 1156–1161, 2019.

[12] S. Yousefizadeh and T. Bak, "Nonlinear disturbance observer for external force estimation in a cooperative robot," in *2019 19th International Conference on Advanced Robotics (ICAR)*. IEEE, 2019, pp. 220–226.

[13] X. Liu *et al.*, "End-effector force estimation for flexible-joint robots with global friction approximation using neural networks," *IEEE Transactions on Industrial Informatics*, vol. 15, no. 3, pp. 1730–1741, 2018.

[14] J. Hu and R. Xiong, "Contact force estimation for robot manipulator using semiparametric model and disturbance kalman filter," *IEEE Transactions on Industrial Electronics*, vol. 65, no. 4, pp. 3365–3375, 2017.

[15] S. Liu, L. Wang, and X. V. Wang, "Sensorless force estimation for industrial robots using disturbance observer and neural learning of friction approximation," *Robotics and Computer-Integrated Manufacturing*, vol. 71, p. 102168, 2021.

[16] P. Song, Y. Yu, and X. Zhang, "A tutorial survey and comparison of impedance control on robotic manipulation," *Robotica*, vol. 37, no. 5, pp. 801–836, 2019.

[17] S. Bruno *et al.*, *Robotics: modelling, planning and control*. Spinger, 2010.

[18] T. Valency and M. Zacksenhouse, "Accuracy/robustness dilemma in impedance control," *J. Dyn. Sys., Meas., Control*, vol. 125, no. 3, pp. 310–319, 2003.

[19] G. S. Fischer *et al.*, "MRI image overlay: application to arthrography needle insertion," *Computer Aided Surgery*, vol. 12, no. 1, pp. 2–14, 2007.

[20] J. Fotouhi *et al.*, "Plan in 2-D, execute in 3-D: an augmented reality solution for cup placement in total hip arthroplasty," *Journal of Medical Imaging*, vol. 5, no. 2, p. 021205, 2018.

[21] A. Shigi *et al.*, "Validation of the registration accuracy of navigation-assisted arthroscopic debridement for elbow osteoarthritis," *Journal of Shoulder and Elbow Surgery*, vol. 28, no. 12, pp. 2400–2408, 2019.

[22] J. Fong, H. Rouhani, and M. Tavakoli, "A therapist-taught robotic system for assistance during gait therapy targeting foot drop," *IEEE Robotics and Automation Letters*, vol. 4, no. 2, pp. 407–413, 2019.

[23] A. Torabi *et al.*, "Application of a redundant haptic interface in enhancing soft-tissue stiffness discrimination," *IEEE Robotics and Automation Letters*, vol. 4, no. 2, pp. 1037–1044, 2019.

[24] A. Mohammadi *et al.*, "Nonlinear disturbance observer design for robotic manipulators," *Control Engineering Practice*, vol. 21, no. 3, pp. 253–267, 2013.

[25] W.-H. Chen *et al.*, "A nonlinear disturbance observer for robotic manipulators," *IEEE Transactions on industrial Electronics*, vol. 47, no. 4, pp. 932–938, 2000.

[26] R. Tao *et al.*, "Modeling and emulating a physiotherapist's role in robot-assisted rehabilitation," *Advanced Intelligent Systems*, vol. 2, no. 7, p. 1900181, 2020.

[27] M. C. Çavuşoğlu, D. Feygin, and F. Tendick, "A critical study of the mechanical and electrical properties of the phantom haptic interface and improvements for high performance control," *Presence: Teleoperators & Virtual Environments*, vol. 11, no. 6, pp. 555–568, 2002.